Superconductivity in textured Bi clusters/Bi2Te3 films

Phuoc Huu Le, Wen-Yen Tzeng, Hsueh-Ju Chen, Chih Wei Luo, Jiunn-Yuan Lin, and Jihperng Leu

Citation: APL Materials **2**, 096105 (2014); doi: 10.1063/1.4894779
View online: http://dx.doi.org/10.1063/1.4894779
View Table of Contents: http://scitation.aip.org/content/aip/journal/aplmater/2/9?ver=pdfcov
Published by the AIP Publishing

Superconductivity in textured Bi clusters/Bi_2Te_3 films

Phuoc Huu Le,[1,2] Wen-Yen Tzeng,[3] Hsueh-Ju Chen,[3] Chih Wei Luo,[3,a] Jiunn-Yuan Lin,[4] and Jihperng Leu[1,b]

[1]*Department of Materials Science and Engineering, National Chiao Tung University, Hsinchu 30049, Taiwan*
[2]*Faculty of Basic Sciences, Can Tho University of Medicine and Pharmacy, 179 Nguyen Van Cu Street, Can Tho, Vietnam*
[3]*Department of Electrophysics, National Chiao Tung University, Hsinchu 300, Taiwan*
[4]*Institute of Physics, National Chiao Tung University, Hsinchu 300, Taiwan*

(Received 30 December 2013; accepted 26 August 2014; published online 4 September 2014)

We report superconductivity at an onset critical temperature below 3.1 K in topological insulator ~200-nm-thick Bi_2Te_3 thin films grown by pulsed laser deposition. Using energy-dispersive X-ray spectroscopy elemental mapping and Auger electron spectroscopy elemental depth profiling, we clearly identified bismuth (Bi) precipitation and Bi cluster signatures. Superconductivity in the Bi_2Te_3 films was attributed to the proximity effect of Bi clusters precipitated on the surface of the Bi_2Te_3 films. [http://dx.doi.org/10.1063/1.4894779]

Bi_2Te_3 is a three-dimensional topological insulator (TI), characterized by an insulating gap in the bulk state and a robust metallic surface or edge state protected by time-reversal symmetry.[1–3] Recent studies have shown that a two-dimensional interface state between TIs and superconductors resulting from the superconducting proximity effect supports Majorana fermions (MFs).[4–7] MFs, novel particles which are their own antiparticles, can potentially be applied to topological quantum computing, which has motivated intense interest in TIs.[7,8] Several approaches to induce superconductivity in TIs have been demonstrated, including doping, application of high pressure, and direct contact with a superconductor by using the proximity effect (PE). Superconductivities in $Cu_xBi_2Se_3$ ($0.1 \leq x \leq 0.3$) and in $Pd_zBi_2Se_3$ ($0.1 \leq z \leq 1$) have been observed with transition temperatures (T_c) of approximately 3.8 and 5.5 K, respectively.[9,10] Moreover, pressure has been applied to successfully induce TIs such as Sb_2Te_3,[11] single crystal Bi_2Te_3,[12–15] polycrystalline Bi_2Te_3,[16] and Bi_4Te_3[17] into a superconducting state.

Recently, the PE has been proposed as a method to study the elusive MF, namely, by combining a superconductor with a TI.[18,19] The PE-induced superconductivity has been demonstrated in Sn–Bi_2Se_3 junction devices, Pb–Bi_2Se_3 interface, and Pb–Bi_2Te_3–Pb sandwich structures through the observation of zero-bias conductance peaks below $T_c \approx 3.8$ K, 1 K, and 7–8 K, respectively.[20–22] In addition, superconductivity ($T_c \approx 3.4$ K) at the In/Bi_2Te_3 interface was induced by indium contacts.[23] Recently, Koren *et al.* observed the local superconductivity in Bi_2Te_2Se and Bi_2Se_3 films below 2–3 K, which was naturally induced by small amounts of superconducting Bi inclusions or precipitations on the surface.[24] In this paper, we report superconductivity in textured Bi_2Te_3 thin films without the use of doping or external pressure, evidently induced by the PE of Bi clusters precipitated on the surface.

A series of Bi_2Te_3 films of various thicknesses were grown on insulating $SrTiO_3$ (STO) (100) substrates by changing deposition time (DT) from 10 to 60 min using pulsed laser deposition (PLD, KrF excimer laser, $\lambda = 248$ nm). The common deposition conditions were as follows: substrate

[a]cwluo@mail.nctu.edu.tw. Tel.: +886-35712121-56196.
[b]jimleu@mail.nctu.edu.tw. Tel.: +886-35131420.

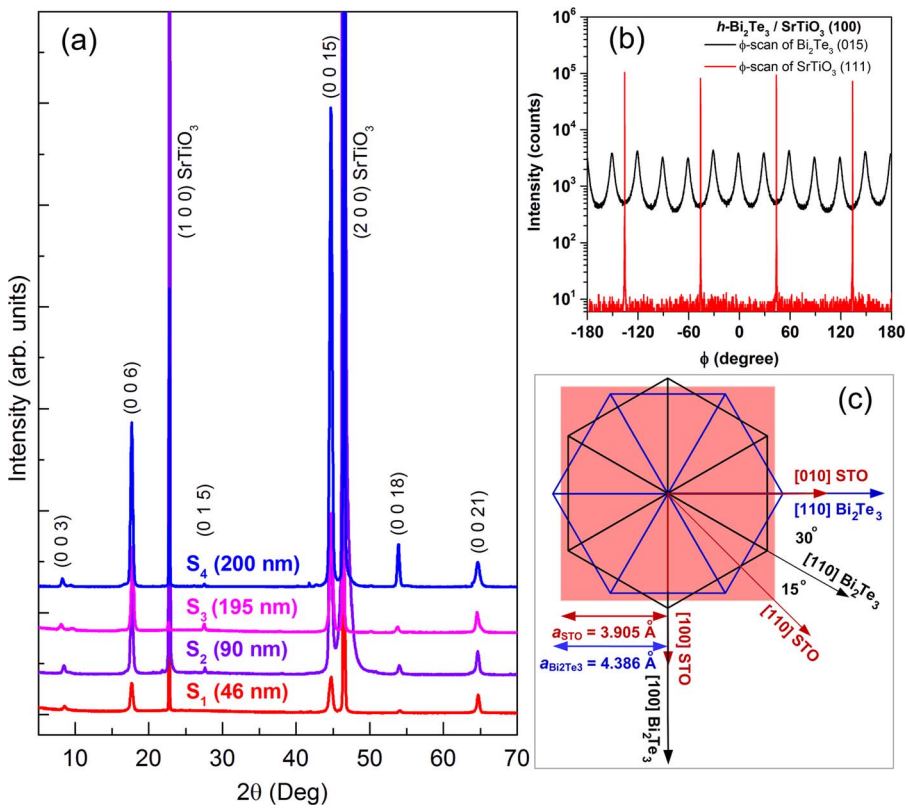

FIG. 1. (a) X-ray diffraction patterns of the Bi_2Te_3 films with various thicknesses from 46 to 200 nm deposited on $SrTiO_3$ (100) substrates. (b) The typical XRD ϕ-scan patterns of the *h*-Bi_2Te_3 thin films grown on $SrTiO_3$ (100) substrates. (c) Schematic of the in-plane arrangement of *h*-Bi_2Te_3/$SrTiO_3$ (100).

temperature: 300 °C; helium ambient pressure: 40 Pa; repetition rate: 2 Hz; and pulsed fluence: approximately 3.4 J/cm^2. In this study, four selected samples are of interests for detail study and discussion, namely, S_1 (thickness = 46 nm, DT = 10 min), S_2 (thickness = 90 nm, DT = 20 min), S_3 (thickness = 195 nm, DT = 60 min), and S_4 (thickness = 200 nm, DT = 60 min).

The orientation of Bi_2Te_3 thin films was determined by using X-ray diffraction (XRD; Bruker D8) with CuK_α radiation ($\lambda = 1.54$ Å) in θ-2θ and ϕ-scan configurations. Temperature-dependent resistivity [$\rho(T)$] and Hall effect measurements were performed with the standard 4-probe technique and silver paste for the contacts in a quantum design physical property measurement system (PPMS) between 1.8 and 300 K. The magnetic field-dependent $\rho(T)$ measurements were achieved with the applied magnetic field along the c-axis ($H_{\|c}$) and the electric currents (10 μA) parallel to the basal plane of the films. The temperature-dependent magnetic susceptibility [$\chi(T)$] was measured at $H_{DC,\|c} = 20$ Oe using a quantum design superconducting quantum interference device (SQUID) system. The energy-dispersive X-ray spectroscopy (EDS) elemental mapping characterization was performed using SEM JEOL JSM-6500—Oxford Instrument detector at 10 kV, a dead time of 5%–6%, and a collecting time of 30 min with 40 frames. Auger Electron Spectroscopy (AES) elemental depth profiling analysis was performed using ThermoVG 350 system under the conditions of low-energy (3 keV) Ar^+ sputtering, electrons raster area of 20 × 30 μm^2, and a beam current of 1 μA.

The θ-2θ scan measurements [Fig. 1(a)] show the dominance of (00l) family planes of the rhombohedral Bi_2Te_3 phase (PDF#82-0358), indicating that the films are highly c-axis-oriented (i.e., textured). In addition, a ϕ-scan [Fig. 1(b)] was conducted on the (015) plane of a 200-nm-thick film (S_4) and the (111) plane of an STO substrate in skew-symmetric geometry by tilting the sample. The in-plane orientation of a hexagonal *h*-Bi_2Te_3/STO (100) film presented 12-fold

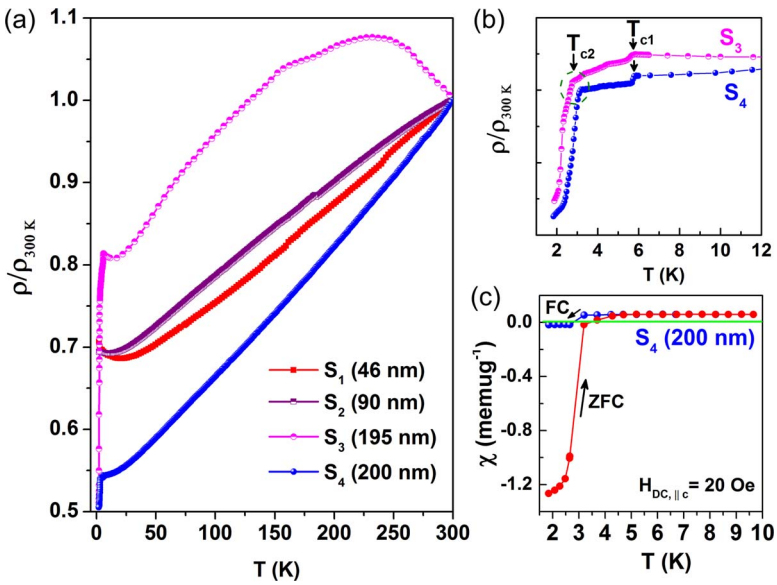

FIG. 2. (a) Temperature-dependent normalized *ab*-resistivities ($\rho/\rho_{300\,K}$) between 1.8 K and 300 K of the Bi_2Te_3 films. (b) Zoomed-in view $\rho/\rho_{300\,K}$ of 195-nm-thick film (S_3) and 200-nm-thick film (S_4) in the low temperature range. (c) Temperature-dependent magnetic susceptibility of S_4 at a magnetic field $H_{DC,\parallel c} = 20$ Oe in zero field cooled (ZFC) and field cooled (FC) measurements.

symmetry instead of the expected six-fold symmetry of the (015) plane in Bi_2Te_3.[25] Fig. 1(c) shows a schematic drawing of the in-plane atomic arrangement between an *h*-Bi_2Te_3 film and an STO (100) substrate. Because the principal crystallographic orientations of *h*-Bi_2Te_3 films grown on STO (100) substrates can be aligned along either the STO [100] or STO [010] directions, the in-plane arrangements result in the observed 12-fold symmetry. The angle differences between STO [010] and the two orientations of *h*-Bi_2Te_3 [110] were 30° and 45°, respectively, as shown in Fig. 1(c). In other words, the in-plane relationships were Bi_2Te_3 [110]//STO [010] and Bi_2Te_3 [100]//STO [100]. Similar results were observed in *h*-$YMnO_3$ films grown on MgO (100) substrates.[26] Using the Williamson-Hall method,[27] the microstrains of a 46-nm-thick film (S_1) and ~200-nm-thick films (S_3, S_4) were estimated to be 0.23% and 0.06%, respectively. Therefore, the strain effect on S_3 and S_4 can be dismissed in this study.

Fig. 2(a) shows the normalized resistivity $\rho/\rho_{300\,K}$ of the films as functions of temperatures (T) from 1.8 to 300 K. Regardless a slightly increased $\rho/\rho_{300\,K}$ of S_3 in 230–300 K, the films show a decrease in $\rho/\rho_{300\,K}$ with decreasing T in the range of 20–300 K, which implies that the films exhibit weak metallic properties commonly seen in narrow band-gap semiconductors with high carrier concentrations.[28] Below 20 K [Figs. 2(a) and 2(b)], the $\rho/\rho_{300\,K}$ of S_1 and S_2 show a gentle upturn because of the weak localization of electrons,[29] whereas the $\rho/\rho_{300\,K}$ of S_3 and S_4 reach a plateau before dropping slightly at $T_{c1} \approx 5.8$ K and then sharply at $T_{c2} \approx 2.8$ K or 3.1 K, respectively. Fig. 2(c) shows the temperature-dependent susceptibilities $\chi(T)$ of S_4 at 20 Oe. Both zero field cooled (ZFC) and FC $\chi(T)$ show a sharp drop at approximately 3.2 K, which is a typical diamagnetic behavior in superconductors.[9,10] The thick Bi_2Te_3 films (i.e., S_3, S_4) prepared using PLD show clear superconducting transitions below 3.1 K.

Figs. 3(a) and 3(b) show the $H_{\parallel c}$-dependent $\rho(T)$ of S_3 and S_4 in low T regime. The onset critical temperature (T_c^{onset}) is determined from the intersection of the two extrapolated lines, as demonstrated in Fig. 3(a). At $H_{\parallel c} = 0$, the T_{c2}^{onset} of S_3 and S_4 were determined to be approximately 2.8 and 3.1 K, respectively. The ρ of the superconducting films drops abruptly by 30% for S_3 and 8% for S_4 below T_{c2}^{onset} but does not go down to zero even at $T = 1.8$ K. This non-zero ρ at low T indicates that the superconducting volume ratio is not 100%.[10,23] On the other hand, the signal of the Meissner effect shown in Fig. 2(c) does suggest the existence of bulk superconductivity. Fig. 3(c) presents magnetic field $H_{\parallel c}$- dependent T_c^{onset} of S_3 and S_4. Clearly, the T_{c2}^{onset} of S_3 (S_4) decreased

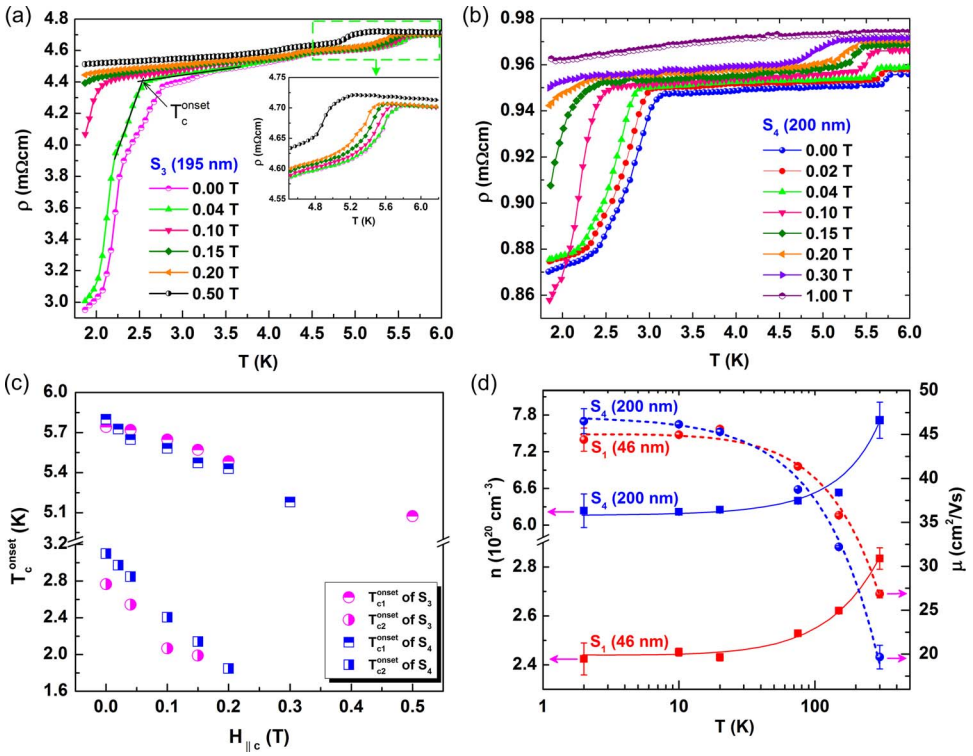

FIG. 3. $\rho(T)$ in 1.75–6.0 K of: (a) 195-nm-thick film (S_3) and (b) 200-nm-thick film (S_4) at various $H_{\parallel c}$ from 0 to 1 T. The inset in (a) shows a zoomed-in-view of the dashed rectangular area of the $\rho(T)$ curves. (c) Onset critical temperatures (T_c^{onset}) of S_3 and S_4 as a function of magnetic field. (d) Temperature-dependent Hall density (n) and mobility (μ) of electrons in the 46-nm- and 200-nm-thick Bi_2Te_3 films. The solid and dashed lines are used to guide the eyes.

from 2.77 (3.10) to 1.99 K (1.85) with increasing $H_{\parallel c}$ from 0 (0) to 0.15 (0.2) T. Also, the T_{c1}^{onset} of S_3 (S_4) decreased from 5.75 (5.80) to 5.07 (5.18) K with increasing $H_{\parallel c}$ from 0 (0) to 0.5 (0.3) T [Fig. 3(c)]. This behavior does indicate that the two transitions are superconducting in nature.

The detail investigations on S_3, S_4 strongly suggest the existence of superconducting Bi nanoclusters on the surface that induces the $T_{c1} \approx 5.8$ K. EDS lateral elemental mapping revealed that the distributions of Te and Bi were not uniform, and many Bi-rich (47–54 at.%) clusters were visible (green color) as shown in Fig. 4(a), differing substantially from the uniform distributions and cluster-free surfaces were observed in S_1 and S_2. The statistical distributions of size (350–2600 nm) and inter-distance (0–5.5 μm) of Bi-rich clusters were obtained from 22 distinctive areas and about 100 clusters on film S_4 by using EDS mapping, as shown in Figs. 4(b) and 4(c). Also, the most probable size (P_s) and inter-distance of Bi-rich clusters are, respectively, in the ranges of 560–772 nm and 1.8–2.4 μm. Moreover, AES analysis shows that the Te/Bi ratio on the surfaces is lower than the expected 3/2 of stoichiometric Bi_2Te_3, indicating that the surface layer is Bi rich [Fig. 4(f), at depth Z = 0]. Because the vapor pressure of Te (at 300 °C) is approximately 10^5 times higher than that of Bi,[30] more Te atoms are re-evaporated from the 300 °C substrates. In addition, the loss of Te is more severe in film S_3, S_4 than in film S_1 [14.3 at.% in S_4 and 4.5 at.% in S_1 at Z = 0, Fig. 4(f)] because of the six to three times longer in deposition time of S_3, S_4 (60 min) than S_1 (10 min) and S_2 (20 min). The nonstoichiometric effect is strongly depth-dependent [Fig. 3(f)]. The Te/Bi ratio gradually increases toward the stoichiometric ratio of 3/2 in ~200-nm-thick films or slightly exceeds it (Te-rich) in the 46-nm-thick film when the depth (Z) of films increases. Under such the sufficiently high surface concentration of Bi atoms, Bi clusters precipitate and segregate readily on the film surfaces to minimize overall free energy,[31] as long as the substrate temperature of 300 °C is higher than the melting point 271 °C of Bi, as demonstrated in Figs. 4(a) and 4(g). Notably, Bi clusters can only be observed in highly Bi-rich films (S_3 and S_4, i.e., by ~14.3 at.% at Z = 0),

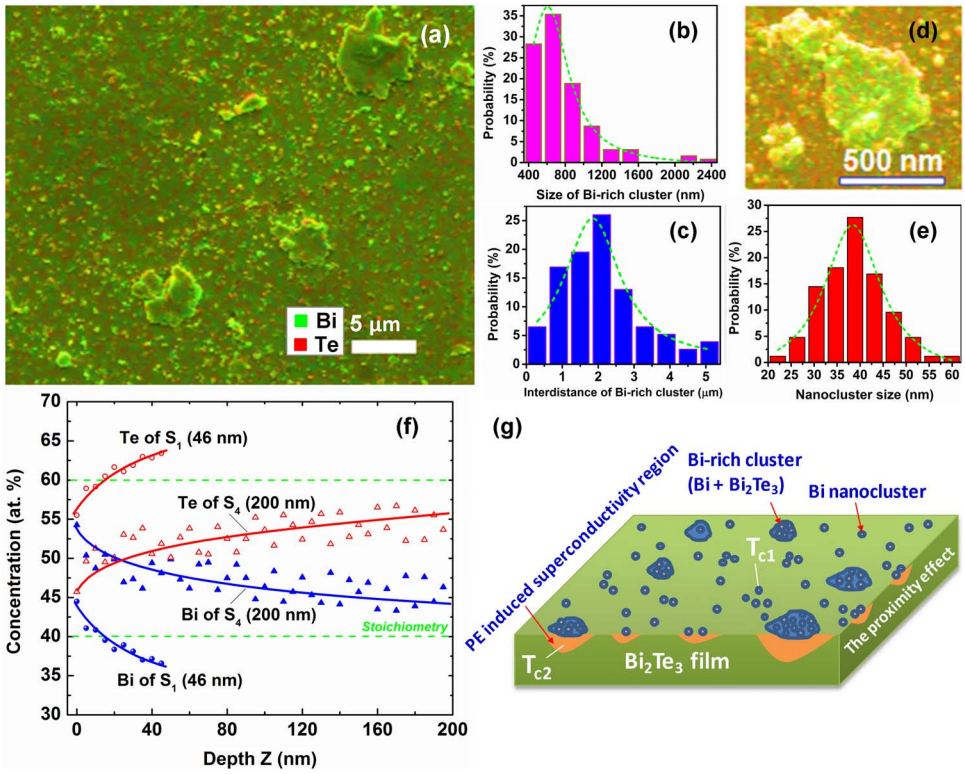

FIG. 4. (a) A typical EDS elemental mapping image [Bi (blue) and Te (red)] of ∼200-nm-thick films. (b) and (c) Size and inter-distance distribution histograms of Bi-rich clusters on the surface of the film. (d) An EDS mapping image of a typical Bi-rich cluster. (e) The size distribution of Bi nanoclusters inside the submicron Bi-rich clusters. (f) AES elemental depth profiling of film S_1 and S_4. (g) Schematics of the surface characteristics and a suggested superconductivity mechanism in the Bi_2Te_3 films.

and not in low Bi-rich films (S_1 and S_2, i.e., by ∼4.5 at.% at Z = 0), suggesting a critical Bi-rich concentration for Bi precipitation (separating a Bi phase) in a Bi_2Te_3 film. Similar Bi precipitation effects have been observed in AlBi alloys[32] and AgBi alloys.[33]

A closer inspection reveals that Bi-rich clusters are composed by some Bi nanoclusters (or nanograins) with size of 20–62 nm and P_s of 36.8–41 nm [Figs. 4(d) and 4(e)]. Fig. 4(d) shows a typical EDS mapping image of the Bi nanoclusters inside a Bi-rich cluster marked by green color. Besides, some of Bi nanoclusters may also spread out of the Bi-rich cluster sites as shown in Figs. 4(a) and 4(g). Recently, Koren *et al.*[24] reported that the T_c of 6.3 K was observed in a Bi_2Te_2Se film with Bi islands on its surface. Therefore, the T_{c1} at approximately 5.8 K found in our samples could be ascribed to the superconducting transition of the Bi nanoclusters. Furthermore, it is also excellently consistent with the local superconductivity in granular Bi nanowires in terms of the T_c value (∼5.8 K), the H-dependent results, and comparable grain size (∼40 nm).[34] The tiny resistivity drop at $T_{c1} \approx 5.8$ K (by approximately 1.7% for S_3 and 0.5% for S_4) [Figs. 3(a), inset and 3(b)] indicates that the amount of superconducting Bi nanoclusters in S_3 and S_4 is likely small and, therefore, the Josephson coupling between these islands is extremely weak. Due to the superconductivity of Bi nanoclusters survived until $H_{\|c} = 1.0$ T [Figs. 3(a) and 3(b)], the critical field of Bi nanoclusters is in between 0.5 and 1.0 T, which is consistent with the critical value of $H_c = 0.55$ T for granular Bi nanowires,[34] but slightly larger than $H_c = 0.45$ T for the Bi powder.[35] It should be noted that Bi nanoclusters and Bi-rich clusters are a kind of thermodynamic defects formed during the growth, the fabrication of the superconducting Bi-rich films is difficult to control and the windows of the growth parameters are narrow. Consequently, the manipulations of size, density, and inter-distance of Bi clusters remain very limited.

The superconductivity of Bi nanoclusters exhibits at $T_{c1} \approx 5.8$ K, what is then the origin of the T_{c2} below 3.1 K. Several possibilities are suggested for the transition at T_{c2}: (1) the existence of other Bi superconducting phases besides the 5.8 K phase, (2) the percolation superconductivity of Bi clusters, and (3) the PE-induced superconductivity of the Bi_2Te_3 film. It is well known that bulk rhombohedral Bi is not superconducting ($T \leq 50$ mK). Under high pressure, however, some phases of Bi, so-called Bi II, III, and V, possess superconductivity with T_c of 3.9, 7.2, and 8.5 K, respectively.[36] Besides, a fcc Bi film deposited on a Ni sublayer shows $T_c \leq 4$ K,[37] and the amorphous Bi exhibits $T_c \approx 6$ K.[34,36] Clearly, the T_{c2} should be unrelated to all of these phases while our Bi_2Te_3 films were grown under an elevated temperature of 300 °C, without applying pressures or considerably strains.

For the percolation superconductivity mechanism, like in granular superconductors, the reduced T_c is due to the lowering of the Josephson coupling energy E_J and dissipation between superconducting grains (or islands).[38] Also, T_c strongly depends on the inter-grain spacing.[39] For example, the T_{c1} (T_{c2}) of the Nb island arrays in Ref. 39 decreased from ~9.2 (9) to ~8.4 (2.5) K with increasing the island spacing from 90 to 340 nm. Due to the substantial nonuniformity of inter-distance between Bi nanoclusters in our Bi_2Te_3 film, it would induce several different T_c to cause the broad transition width for T_{c1} and T_{c2} rather than the sharp transition ($\Delta T_{c1} < 0.4$ K, $\Delta T_{c2} < 0.6$ K) as we observed in Figs. 3(a) and 3(b).

Recently, Koren *et al.* observed that the superconductivity below 2–3 K in Bi_2Se_3 and Bi_2Te_2Se films, which was attributed to proximity-induced local superconductivity by small amounts of superconducting Bi inclusions or segregation to the surface with T_c of 6.3 K.[24] Furthermore, the strong superconducting proximity effect in Pb–Bi_2Te_3–Pb hybrid structures was also reported,[22] in which a supercurrent can be established through 100–300-nm-thick Bi_2Te_3 flakes at a temperature of ~7.2 K. Also, it has been observed that PE-induced superconducting state in Bi_2Se_3 exists over an extended distance of ~1 μm away from the Pb-Bi_2Se_3 interface.[21] In regard to this mechanism, the induced superconducting regions [(adjacent to the Bi clusters/Bi_2Te_{-3} interfaces, orange regions in Fig. 4(g)] can be established inside the Bi_2Te_3 films. The PE-induced superconducting volume of T_{c2} is expected to be larger than that of Bi nanoclusters with T_{c1} and further cause the larger resistivity drops (i.e., 30% vs. 1.7% for S_3, and 8% vs. 0.5% for S_4), as shown in Figs. 3(a) and 3(b). Consequently, the T_{c2} (2.8 or 3.1 K, at 0 T) in the Bi_2Te_3 films is relatively distinctive, stable, and reproducible, suggesting the PE-induced superconductivity may dominate the transition at T_{c2}.

The temperature-dependent $\rho/\rho_{300\,K}$ in Fig. 2(a) can be understood as a result of the competition between temperature-dependent carrier concentration (n) and carrier mobility (μ) in determining the resistivity $\rho = 1/ne\mu$. The films in this study are n-type [confirmed by Hall effect measurements on S_1 and S_4, Fig. 3(d)] and, therefore, the dominant defect is V_{Te} (Te-vacancy) under the Bi-rich condition (or Te-deficiency),[40] which donates electrons to the conduction band and results in the high background carrier concentrations even at 2 K up to $n_{S1} = 2.4 \times 10^{20}$ cm^{-3} and $n_{S2} = 6.2 \times 10^{20}$ cm^{-3}. Because of the freeze-out of carriers resulting from cooling [from 300 to 2 K in Fig. 3(d)], the carrier concentrations of S_1 and S_4 slightly decreased from 2.8×10^{20} to 2.4×10^{20} cm^{-3} (14.3% reduction) and from 7.7×10^{20} to 6.2×10^{20} cm^{-3} (19.5% reduction), respectively, which is consistent with observations of Bi_2Te_3[41] and Bi_2Se_3 films.[42] Moreover, the mobility (μ) of both S_1 and S_4 substantially increased as the temperature decreased to 20 K. Below 20 K in S_1, the slight decrease in μ likely occurs because of ionized impurity scattering, which results in the increase in $\rho/\rho_{300\,K}$ below 20 K [Fig. 2(a)]. Conversely, the $\rho/\rho_{300\,K}$ plateau below 20 K in S_4 was due to the weakly T-dependent μ and n [Figs. 2(b) and 3(d)].

In summary, superconductivity was observed with onset $T_c \leq 3.1$ K in ~200-nm-thick Bi_2Te_3 thin films grown using PLD. The Bi_2Te_3 films were highly c-axis oriented and epitaxially grown on STO (100) substrates with in-plane relationships of Bi_2Te_3 [110]//STO [010] and Bi_2Te_3 [100]//STO [100]. The precipitation of Bi-rich clusters on the surface of thick Bi_2Te_3 films was identified using AES depth profiling and EDX mapping characterization. This study demonstrates that natural defects generated during growth, namely, superconducting Bi nanoclusters or Bi inclusions, can substantially induce a nonsuperconducting TI thin film (Bi_2Te_3) into a superconducting state at low temperatures.

Financial support from the National Science Council of the Republic of China (Taiwan) under Contract Nos.: NSC101-2221-E-009-126-MY2, NSC 101-2112-M-009-016-MY2, NSC 101-

2112-M-009-017-MY2, MOST 103-2628-M-009-002-MY3, MOST 103-2221-E-009-181-MY3, and MOST 103-2119-M-009-004-MY3 is gratefully acknowledged.

[1] Y. L. Chen, J. G. Analytis, J.-H. Chu, Z. K. Liu, S.-K. Mo, X. L. Qi, H. J. Zhang, D. H. Lu, X. Dai, Z. Fang, S. C. Zhang, I. R. Fisher, Z. Hussain, and Z.-X. Shen, Science **325**, 178 (2009).
[2] H. Zhang, C.-X. Liu, X.-L. Qi, X. Dai, Z. Fang, and S.-C. Zhang, Nat. Phys. **5**, 438 (2009).
[3] L. Fu, C. Kane, and E. Mele, Phys. Rev. Lett. **98**, 106803 (2007).
[4] P. G. De Gennes, *Superconductivity of Metals and Alloys* (Benjamin, New York, 1966).
[5] L. Fu, and C. Kane, Phys. Rev. Lett. **100**, 096407 (2008).
[6] X.-L. Qi, T. Hughes, S. Raghu, and S.-C. Zhang, Phys. Rev. Lett. **102**, 187001 (2009).
[7] F. Wilczek, Nat. Phys. **5**, 614 (2009).
[8] C. Nayak, A. Stern, M. Freedman, and S. D. Sarma, Rev. Mod. Phys. **80**, 1083 (2008).
[9] Y. S. Hor, A. J. Williams, J. G. Checkelsky, P. Roushan, J. Seo, Q. Xu, H. W. Zandbergen, A. Yazdani, N. P. Ong, and R. J. Cava, Phys. Rev. Lett. **104**, 057001 (2010).
[10] Y. S. Hor, J. G. Checkelsky, D. Qu, N. P. Ong, and R. J. Cava, J. Phys. Chem. Solids **72**, 572 (2011).
[11] J. Zhu, J. L. Zhang, P. P. Kong, S. J. Zhang, X. H. Yu, J. L. Zhu, Q. Q. Liu, X. Li, R. C. Yu, R. Ahuja, W. G. Yang, G. Y. Shen, H. K. Mao, H. M. Weng, X. Dai, Z. Fang, Y. S. Zhao, and C. Q. Jin, Sci. Rep. **3**, 2016 (2013).
[12] C. Zhang, L. Sun, Z. Chen, X. Zhou, Q. Wu, W. Yi, J. Guo, X. Dong, and Z. Zhao, Phys. Rev. B **83**, 140504(R) (2011).
[13] J. L. Zhang, S. J. Zhang, H. M. Weng, W. Zhang, L. X. Yang, Q. Q. Liu, S. M. Feng, X. C. Wang, R. C. Yu, L. Z. Cao, L. Wang, W. G. Yang, H. Z. Liu, W. Y. Zhao, S. C. Zhang, X. Dai, Z. Fang, and C. Q. Jin, Proc. Natl. Acad. Sci. U.S.A. **108**, 24 (2011).
[14] S. J. Zhang, J. L. Zhang, X. H. Yu, J. Zhu, P. P. Kong, S. M. Feng, Q. Q. Liu, L. X. Yang, X. C. Wang, L. Z. Cao, W. G. Yang, L. Wang, H. K. Mao, Y. S. Zhao, H. Z. Liu, X. Dai, Z. Fang, S. C. Zhang, and C. Q. Jin, J. Appl. Phys. **111**, 112630 (2012).
[15] L. Zhu, H. Wang, Y. Wang, J. Lv, Y. Ma, Q. Cui, Y. Ma, and G. Zou, Phys. Rev. Lett. **106**, 145501 (2011).
[16] M. Einaga, Y. Tanabe, A. Nakayama, A. Ohmura, F. Ishikawa, and Y. Yamada, J. Phys.: Conf. Ser. **215**, 012036 (2010).
[17] J. R. Jeffries, A. L. Lima Sharma, P. A. Sharma, C. D. Spataru, S. K. McCall, J. D. Sugar, S. T. Weir, and Y. K. Vohra, Phys. Rev. B **84**, 092505 (2011).
[18] P. Zareapour, A. Hayat, S. Y. F. Zhao, M. Kreshchuk, A. Jain, D. C. Kwok, N. Lee, S. Cheong, Z. Xu, G. D. Gu, S. Jia, R. J. Cava, and K. S. Burch, Nat. Commun. **3**, 1056 (2012).
[19] T. D. Stanescu, J. D. Sau, R. M. Lutchyn, and S. Das Sarma, Phys. Rev. B **81**, 241310 (2010).
[20] F. Yang, Y. Ding, F. Qu, J. Shen, J. Chen, Z. Wei, Z. Ji, G. Liu, J. Fan, C. Yang, T. Xiang, and L. Lu, Phys. Rev. B **85**, 104508 (2012).
[21] F. Yang, F. Qu, J. Shen, Y. Ding, J. Chen, Z. Ji, G. Liu, J. Fan, C. Yang, L. Fu, and L. Lu, Phys. Rev. B **86**, 134504 (2012).
[22] F. Qu, F. Yang, J. Shen, Y. Ding, J. Chen, Z. Ji, G. Liu, J. Fan, X. Jing, C. Yang, and L. Lu, Sci. Rep. **2**, 339 (2012).
[23] J. A. Hagmann, X. Liu, M. Dobrowolska, and J. K. Furdyna, J. Appl. Phys. **113**, 17C724 (2013).
[24] G. Koren, T. Kirzhner, E. Lahoud, K. Chashka, and A. Kanigel, Phys. Rev. B **84**, 224521 (2011).
[25] J. E. Brom, Y. Ke, R. Du, D. Won, X. Weng, K. Andre, J. C. Gagnon, S. E. Mohney, Q. Li, K. Chen, X. X. Xi, and J. M. Redwing, Appl. Phys. Lett. **100**, 162110 (2012).
[26] K. H. Wu, H.-J. Chen, Y. T. Chen, C. C. Hsieh, C. W. Luo, T. M. Uen, J. Y. Juang, J.-Y. Lin, T. Kobayashi, and M. Gospodinov, Eurphys. Lett. **94**, 27006 (2011).
[27] G. K. Williamson and W. H. Hall, Acta Metall. **1**, 22 (1953).
[28] Y. Hor, A. Richardella, P. Roushan, Y. Xia, J. Checkelsky, A. Yazdani, M. Hasan, N. Ong, and R. Cava, Phys. Rev. B **79**, 195208 (2009).
[29] Y. Onose, R. Yoshimi, A. Tsukazaki, H. Yuan, T. Hidaka, Y. Iwasa, M. Kawasaki, and Y. Tokura, Appl. Phys. Express **4**, 083001 (2011).
[30] H. Noro, K. Sato, and H. Kagechika, J. Appl. Phys. **73**, 1252 (1993).
[31] D. L. Smith, *Thin-Film Deposition: Principles and Practice* (McGraw-Hill, New York, 1995).
[32] Anawati, H. Nordmark, S. Diplas, J. C. Walmsley, and K. Nisancioglu, J. Electrochem. Soc. **159**, C137 (2012).
[33] V. A. Safonov, M. A. Choba, and M. I. Buleev, Russ. J. Electrochem. **48**, 163 (2012).
[34] M. Tian, N. Kumar, M. H. W. Chan, and T. E. Mallouk, Phys. Rev. B **78**, 045417 (2008).
[35] L. A. Baring, R. R. da Silva, and Y. Kopelevich, Low Temp. Phys. **37**, 889 (2011).
[36] B. Weitzel and H. Micklitz, Phys. Rev. Lett. **66**, 385–388 (1991).
[37] J. S. Moodera and R. Meservey, Phys. Rev. B **42**, 179–183 (1990).
[38] K. Yamada, H. Fujiki, B. Shinozaki, and T. Kawaguti, Physica C **355**, 147–155 (2001).
[39] S. Eley, S. Gopalakrishnan, P. M. Goldbart, and N. Mason, Nat. Phys. **8**, 59–62 (2012).
[40] A. Hashibon and C. Elsässer, Phys. Rev. B **84**, 144117 (2011).
[41] S. X. Zhang, L. Yan, J. Qi, M. Zhuo, Y.-Q. Wang, R. P. Prasankumar, Q. X. Jia, and S. T. Picraux, Thin Solid Films **520**, 6459 (2012).
[42] H. D. Li, Z. Y. Wang, X. Kan, X. Guo, H. T. He, Z. Wang, J. N. Wang, T. L. Wong, N. Wang, and M. H. Xie, New J. Phys. **12**, 103038 (2010).